Title: Forensic Determination of Residual Stresses and K_I from Fracture Surface Mismatch

Author(s):
Prime, Michael B.
DeWald, Adrian T.
Hill, Michael R.
Clausen, Bjorn
Tran, Minh

Details: Engineering Fracture Mechanics, 2014, Vol. 116, pp. 158-171.

DOI: 10.1016/j.engfracmech.2013.12.008

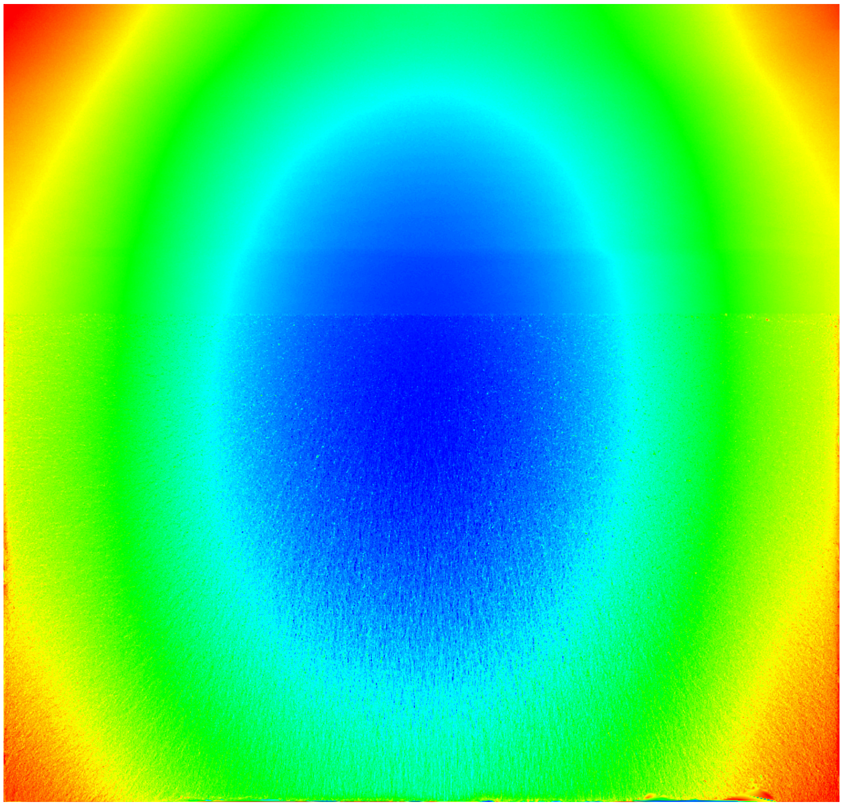

Forensic Determination of Residual Stresses and K_I from Fracture Surface Mismatch

Michael B. Prime[1*], Adrian T. DeWald[2], Michael R. Hill[3], Bjørn Clausen[1], Minh Tran[3]

1. Los Alamos National Laboratory, Los Alamos, NM 87545
2. Hill Engineering, LLC, Rancho Cordova, CA 95670
3. Mechanical and Aerospace Engineering Department, University of California, Davis, CA, 95616
* Corresponding author. prime@lanl.gov, voice: +1-505-667-1051

Abstract

Residual stresses can be a main cause of fractures, but forensic failure analysis is difficult because the residual stresses are relaxed after fracture because of the new free surface. In this paper, a method is presented for *a posteriori* determination of the residual stresses by measuring the geometric mismatch between the mating fracture surfaces. Provided the fracture is not overly ductile, so that plasticity may be neglected, a simple, elastic calculation based on Bueckner's principle gives the original residual stresses normal to the fracture plane. The method was demonstrated on a large 7000 series aluminum alloy forging that fractured during an attempt to cut a section into two pieces. Neutron diffraction measurements on another section of the same forging convincingly validated the residual stresses determined from the fracture surface mismatch. After accounting for closure, an analysis of the residual stress intensity factor based on the measured residual stress agreed with the material's fracture toughness and fractographic evidence of the failure initiation site. The practicality of the fracture surface method to investigate various failures is discussed in light of the required assumptions.

Keywords: fracture, residual stress, fractography, failure analysis, fracture surface mismatch, conjugate surface, crack closure, aluminum

1. Introduction

The influence of residual stresses on failures caused by fatigue, fracture, stress-corrosion cracking, embrittlement, buckling, and other failure processes has been well documented [1-4].

In an actual failed part, there is no current technology for determining the residual stresses that originally existed and contributed to the failure. It is well known that "in the vicinity of the crack, the residual stress is in part or completely relieved in the direction normal to the crack line [5]." Because of that, "testing of undamaged similar, or exemplar parts, is frequently used as the only alternative in order to understand the residual stress system in the failed part prior to fracture [3]." Although useful, such testing of similar parts is inherently limited because the residual stresses may not be the same. Sometimes, there is a question if the failed part might have missed a processing step or may be an outlier in some way. Also, residual stresses can change in service because of fatigue loading, high static loading, and thermal excursions that may not be known. Furthermore, it may not be possible to reproduce similar parts because of lost records or changed processes.

This paper presents an experimental, forensic approach to determine the residual stresses in a part that has failed under brittle conditions. The residual stresses that will be determined are those that existed prior to the fracture and along what became the fracture surface. These are precisely the stresses that may have contributed to mode I fracture and thus could be invaluable in failure analysis. The approach is demonstrated on a large 7000 series aluminum alloy forging that fractured during an attempt to cut a section into two pieces and validated with residual stresses measured on another section of the same forging using neutron diffraction.

2. Principle

The slight misfit between mating fracture surfaces will be measured and used to determine the residual stresses that, prior to fracture, existed at the fracture location.

A finite element (FE) model is used to illustrate and verify the principle and investigate some simplifications. A two-dimensional model is used for illustrative purposes, but the principle is valid in three dimensions as will be demonstrated experimentally later. Figure 1 shows the model of a beam 3 units long by 1 unit thick. The mesh (not shown) of 8-noded, quadratic shape function quadrilateral plane strain elements included a pre-determined crack that divided the beam roughly in half lengthwise. The beam is assumed to behave elastically, with an elastic modulus of 10 and Poisson's ratio of 0.3. Figure 1a shows the initial longitudinal residual stress (σ_x) in what is taken as the undeformed state of the beam. In the central region of the beam, the stresses vary parabolically from +1 at the top and bottom surfaces to -1/2 at the core. The stresses decay smoothly to zero at the ends to satisfy the free surface conditions. All other stress components are zero in the central region of the beam and finite in the stress gradient regions as needed to satisfy the equilibrium conditions. The nodes along the opposing surfaces of the crack line are initially bonded together. During the FE analysis the bonds are removed as desired, and an equilibrium analysis is used to determine the elastic deformation and re-distribution of stresses. To allow a general discussion, Figure 1b shows an arbitrary intermediate state with a partial crack and Figure 1c shows the beam after complete fracture.

2.1. Assumptions and theoretical observations

It is first assumed that the part of interest is fractured cleanly in two in a brittle fracture process without significant plasticity and that no material is removed by the fracture process. Under such circumstances, conventional wisdom would lead one to expect that the fracture surfaces fit together perfectly. Figure 1c illustrates that elastic relaxation of residual stresses causes a mismatch. In the region that had been under tensile residual stresses, the surfaces have pulled away from each other. In the compressive stress region, the surfaces have moved closer.

The free surface boundary condition requires that the stress normal to the new free surface equal zero. Although the direction of the free surface normal varies along the crack path, the average normal is in the longitudinal direction so the longitudinal stress has relaxed to near zero along the crack.

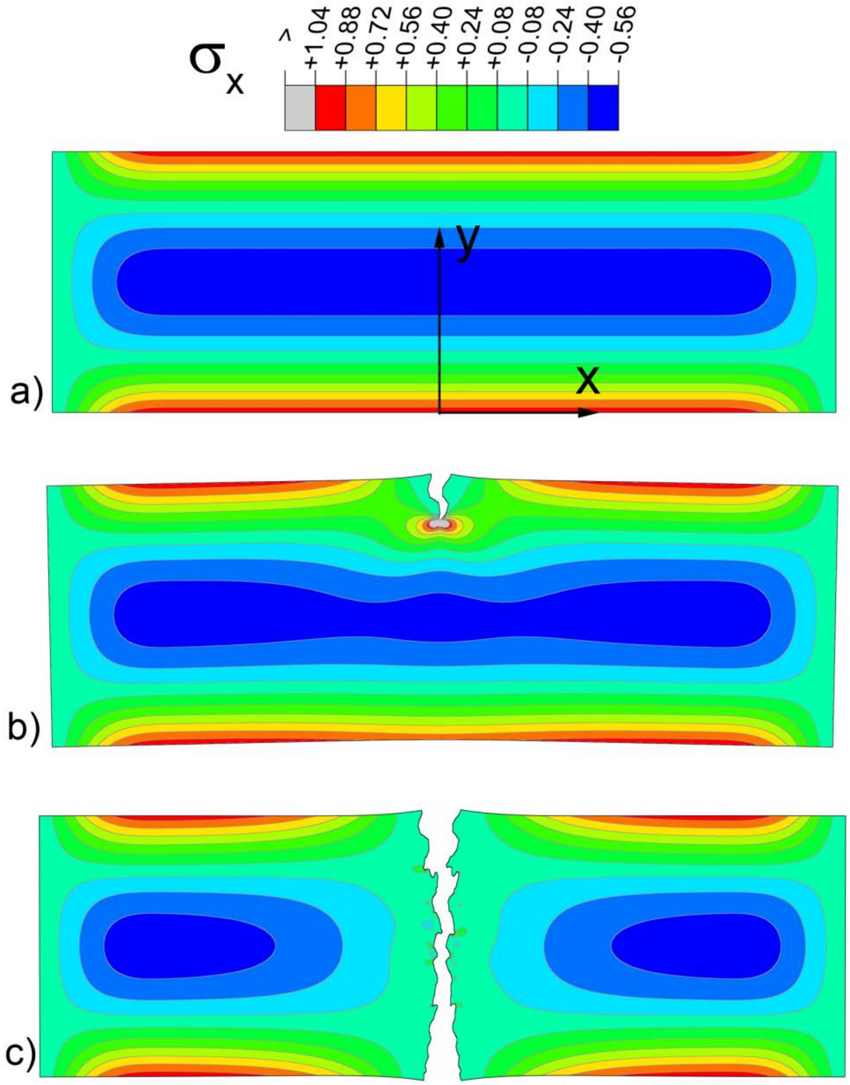

Figure 1. Longitudinal (x) residual stress in an a) intact beam, b) partially cracked beam and c) fractured beam. The stresses redistribute elastically as the free surface is exposed.

The misfit between the surfaces can be determined from surface height maps, or contours, of the opposing fracture surfaces. Figure 2 shows the contours for the deformed surfaces from Figure 1c, where $y = 0$ corresponds to the bottom surface of the beam. When the two contours are averaged the geometrical features of the jagged fracture surface average away leaving half of the misfit. The reference line (reference plane in 3-D) for surface heights is arbitrary, leaving the reference arbitrary in the average as well.

It will be useful to interpret the misfit in terms of displacement of points on the fracture surface. Considering that points on the opposing surfaces were originally coincident, the half misfit equals the average x-displacement of opposing points taken as positive in the outward x-direction from each surface.

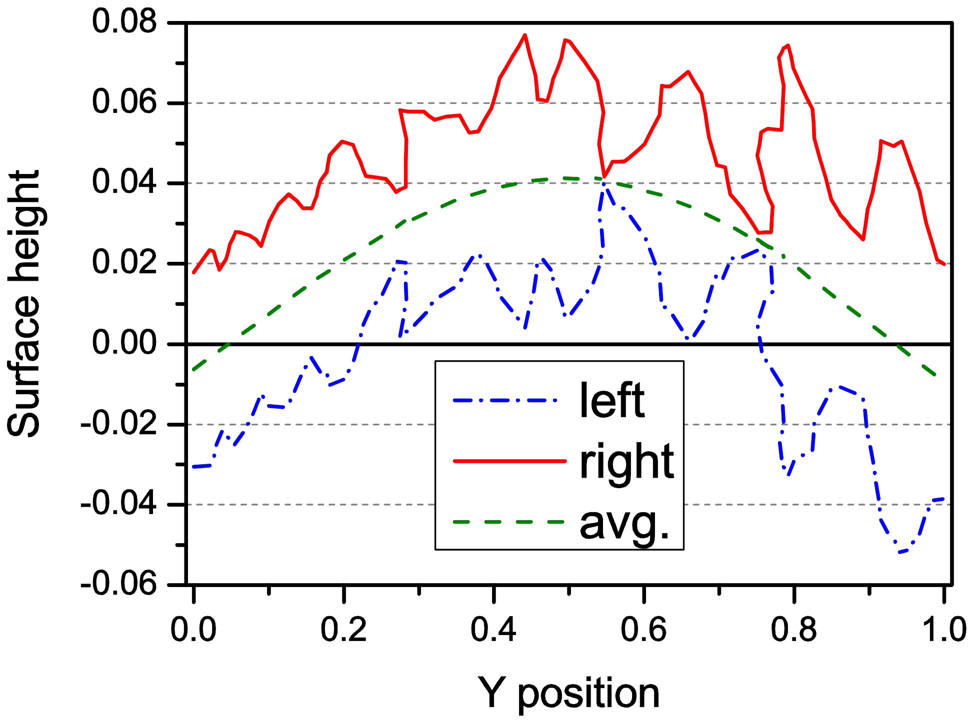

Figure 2. The surface heights measured on the two halves of the beam in Figure 1c can be averaged to reveal the half-misfit between the two surfaces.

Bueckner [6] showed that in spite of the redistribution of stresses throughout a cracked body, the elastic problem can be reduced to one of tractions distributed over faces of the crack [7].[1] The *change* in deformation and stress between any two states in the crack problem, such as a–b, a–c, or b–c in Figure 1, is uniquely and completely determined by applying the relevant residual stresses in the first state as tractions on the crack surface in the second state. The relevant stresses are $\sigma_{x'}$ and $\tau_{x'y'}$ in Figure 1 (and $\tau_{x'z'}$ in the 3D case) along the fracture path where *x*′ is the local surface normal. Other stress components and stresses elsewhere can change but they have no direct influence on the problem of interest (indirectly, all the stresses are interrelated through the equilibrium conditions).

2.2. Stress calculation

The inverse problem calculating the residual stresses from the misfit is solved using the variation on Bueckner’s principle that is used for the contour method for measuring residual stress [10]. In the contour method, a part is carefully cut in two and the contours of the two surfaces created by the cut are measured, averaged, and used to calculate the residual stresses. Applying the same principle to the fracture surface problem, the residual stresses are calculated by forcing the fracture surface back to its

---

[1] Bueckner proved the superposition principle but did not publish figures similar to those in this paper and others. Following Buckner’s work, such figures started appearing soon after [8]. Although the principle was unproven, similar figures had also appeared prior [9].

undeformed configuration: applying the opposite of the displacements of the fracture surface to that surface and calculating the change in stress.

In this section, the FE model will be used to first demonstrate an exact application of Bueckner's principle to the fracture problem, then to demonstrate the approximations for practical implementation of the approach.

Figure 3 illustrates application of Bueckner's principle for calculating the residual stress in Figure 1a. In order to illustrate the exact principle, both x and y displacements from the FE simulation of Figure 1 have been applied to the model (the x-displacements are the same as the half-misfit of Figure 2). Because the displacements are small for engineering materials, the convenient approximation has been made to start from an undeformed model and force it into the opposite of the deformed shape. Bueckner's principle gives

$$\sigma_x(x,y,z) = \sigma'_x(x,y,z) + \sigma''_x(x,y,z) \tag{1}$$

Where σ refers to the original stress state (Figure 1a for this example) σ' is the relaxed stress state, Figure 1c, and σ'' is the *change* in stress, σ - σ', which is calculated in Figure 3. Since σ'_x is approximately zero on the cut surface, σ''_x on the cut surface in Figure 3 is very nearly equal to the original stresses. A slight difference occurs because the local surface normal on the cut surface departs from the x-direction so σ'_x is not precisely zero.

Two approximations are made to experimentally implement this approach. First, the transverse (y) displacements are not applied to the fracture surface because they are not determined by the averaged contour. Second, the fracture surface is meshed as planar rather than trying to mesh the fine geometrical detail. These two approximations are illustrated in Figure 4. To illustrate the generality of the approach, this time the partially cracked body in Figure 1b is taken as the "original" state, so the displacements are only applied to the portion of the fracture plane that was still uncracked in Figure 1b. The normal displacements applied are those determined by averaging the measured surface contours, Figure 2. Because y-displacements are unconstrained, a single node is constrained in the y-direction to prevent rigid body translation. The stresses along the fracture plane in Figure 4 match those along the fracture plane in Figure 1b. Although not plotted here because of space considerations, applying the average contour from Figure 2 along the entire surface of the model in Figure 4 returns the original residual stresses from Figure 1a.

2.3. Further theoretical details

Shear stresses released on the fracture plane, τ_{xy} and τ_{xz}, will affect the measured contours. Because the effect of shear stress is anti-symmetric, averaging the two contours removes the effect, and the normal stress is calculated without error [10]. The shear stresses cause a transverse-direction misfit in the fracture surfaces, which is addressed in the Discussion section. For the calculation of the normal stress on the fracture plane, Bueckner's principle dictates that no assumptions need to be made about any of the other stress components. The other stress components do change, and are discussed in more detail elsewhere [11].

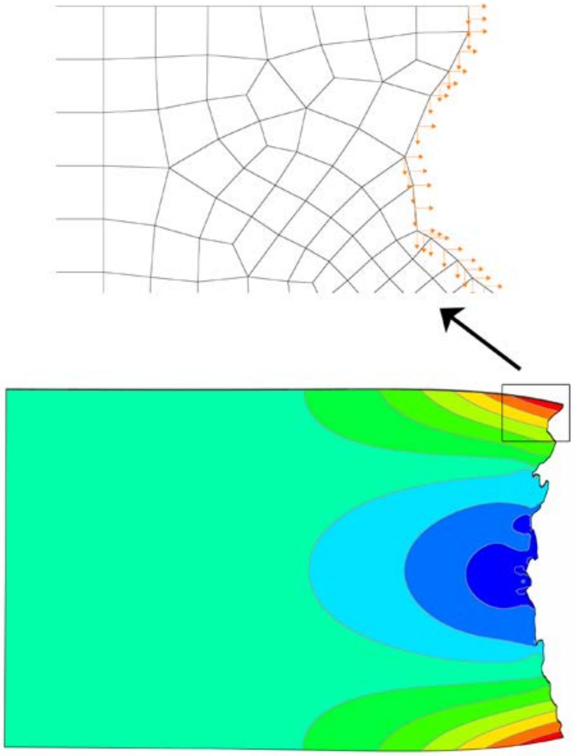

Figure 3. Applying both x and y displacements to the fractured surface (top) to force it into the opposite of the measured shape and calculate stress (bottom). Deformed shape exaggerated by a factor of two. Same color scale as Figure 1.

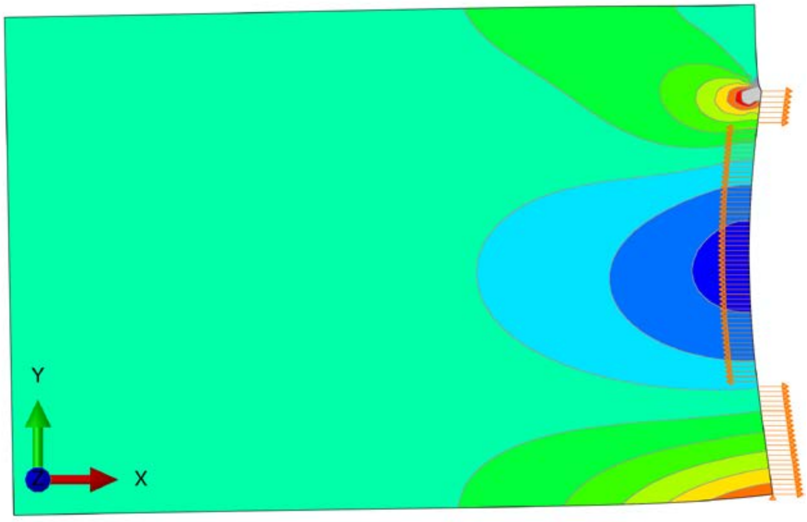

Figure 4. Applying the average contour from Figure 2 as x-displacements to only part of the surface gives the stress state of the partially cracked body, Figure 1b. Same color scale as Figure 1.

The consequence of approximating the fracture surface as flat in the FE model used for stress calculation will depend on how much the actual fracture surface departs from planarity and the length scale of the stress gradients. The numerical example illustrated in Figure 4 shows that the effect is modest (and in fact helpful in that case), for a surface with a root-mean-square surface roughness of about 1.2% of the part thickness.

The measured misfit contains an arbitrary rigid body motion, which does not affect the stress calculation [10]. The residual stresses must satisfy force and moment equilibrium, which allows the FE calculation to take care of the rigid body motion. For example, the free end (left) of the beam in Figure 4 would translate and rotate as necessary for the stresses to satisfy equilibrium.

The elastic problem is path independent, which is why the principle can be applied between any two states, such as at different crack lengths. Therefore, the result is also independent of applied loads that may have been part of the fracture, unless the applied load led to plasticity. The procedure will only determine the residual stresses, not the stresses from the load. The elastic assumption only means that the stress relaxation after the fracture process is elastic, the source of the original residual stresses can be from plastic deformation.

3. Specimen

3.1. Material

The subject is an aluminum alloy hand forging, 1.82 m long, with a cross-section 209 mm by 207 mm (Figure 5). A cylindrical billet of 7050 alloy, 584 mm in diameter, was hand forged at high temperature (600 to 820° F) in open dies, by drawing along the length and squeezing alternately along two orthogonal transverse directions, until the desired cross-section was reached. The total reduction of cross sectional area was 84%. Following forging, the subject was solution heat treated and quenched to T74 condition according to AMS 2772E. In typical practice, a mechanical stress relief (elastic-plastic stretch along the length or bite compression on the transverse) follows quench, but the subject was not stress relieved. Measured tensile properties are typical of 7050-T74 (yield strength along L, LT, and ST of 453, 442, and 431 MPa, respectively, and ultimate strength along L, LT, and ST of 519, 501, and 493 MPa, respectively).

3.1. Fracture

A 196 mm long section was cut without incident from the forging with a band saw. Using a wire EDM equipped with 0.010 inch diameter wire, another cut on the section was attempted with the wire oriented along the *y*-direction and the cut progressing in the -*z* direction (Figure 5). Spontaneous fracture occurred at a cut length of approximately 76.5 mm. Immediately following fracture, the EDM cut was terminated and the specimen was removed from the EDM to preserve the fracture surfaces. A photograph of one of the fracture surfaces is shown in Figure 6.

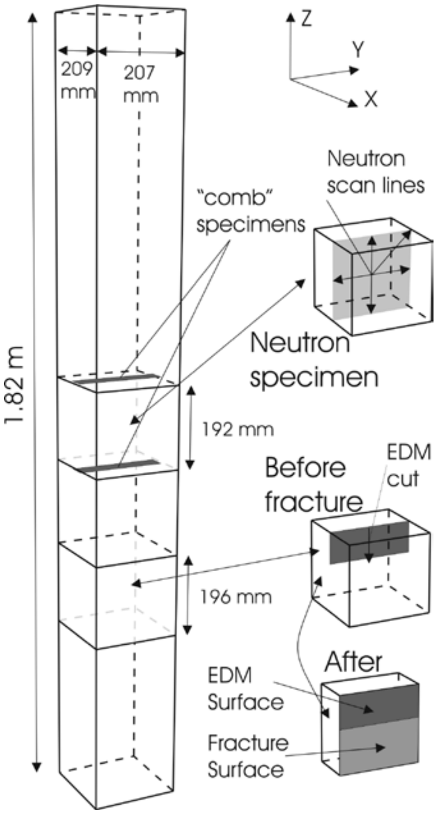

Figure 5. Schematic of forging and specimens that were removed.

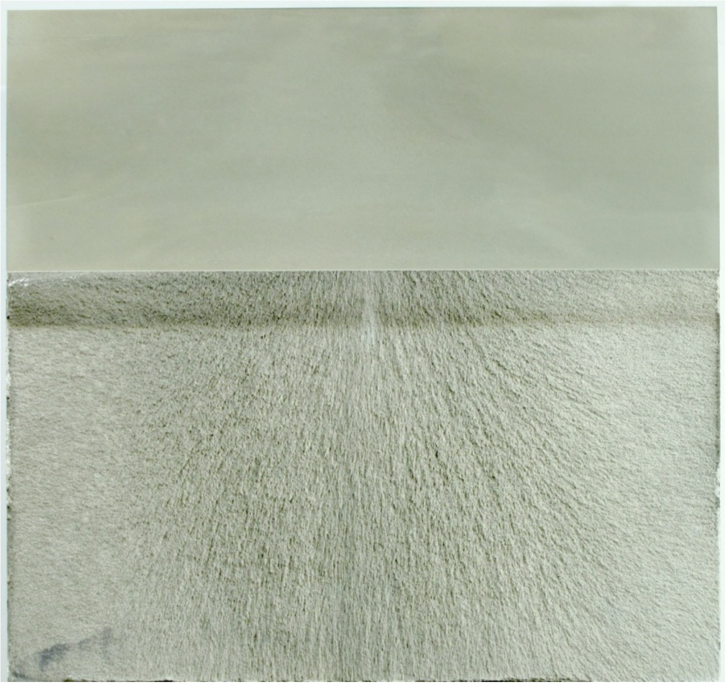

Figure 6. Photograph of fracture surface. The top ≈ 40% of the picture is the EDM cut.

4. Methods

4.1. Surface height and misfit measurement

A surface height map of the part over the EDM cut and fracture plane was measured using a scanning profilometer equipped with a triangulation based laser displacement gage. The measurements were taken at a regular grid of points with 100 µm point spacing. This resulted in roughly 4 million data points on each surface. For ease of plotting and processing, each surface was translated and rotated such that the best-fit plane was at a constant height of zero.

Following measurement, the surfaces were carefully aligned relative to one another by looking at a plot of the misfit. As the alignment improves, the misfit becomes more smooth (i.e., less like a fracture surface) and the alignment was iterated until the fit was optimized by eye to within the 100 µm point spacing. The portion of the surface contour that was cut using wire EDM was shifted in the x-direction by an amount equal to one-half of the cut-width to align it with the fracture portion, which has zero cut-width. The shift is necessary to obtain the correct results when calculating stresses over the whole surface as in Figure 3.

4.2. FEM Contour Stress Calculation

A 3D elastic FE model was used to calculate the stresses from the surface contour data. The model of half of the rectangular block used 200,000 linear shape-function hexahedral elements. The elements were approximately cubes 1.0 mm on a side near the fracture surface and the mesh was graded to be coarser farther away. Elastic properties for 7050-T74 were taken to be modulus of 71.7 GPa and Poisson’s ratio of 0.33.

Converting the raw data into a form suitable for stress calculation followed standard procedure for the contour method [12, 13]. The two fracture surface contours were averaged. The resulting average contour was then smoothed using quadratic bivariate spline fits. The optimal knot spacing for the splines was determined by minimizing the estimated uncertainty in the stresses [12]. The smoothed surface was evaluated at nodal coordinates in order to apply normal (x) displacement boundary conditions to the FE model and deform the cut surface into the opposite of the measured half-misfit [10].

4.3. Neutron Diffraction

To validate the residual stresses determined from the fracture surfaces, neutron diffraction measurements were made on another sample taken from the same forging, see Figure 5.

Using the SMARTS instrument [14] at the Los Alamos Neutron Science Center (LANSCE), measurements were made along the three scan lines shown in Figure 5 with the sampling volume confined to $5\times5\times4$ mm^3 using incident slits (5x5 mm^2) and radial collimators (4 mm). Spacing between locations was 6 mm for the horizontal (along y) and vertical (along z) scans and 9 mm for the diagonal scan for a total of about 80 measurement locations. Measurements were made in two orientations to get strains in the x, y, and z directions at each point. Because of the large specimen size, less than 5% neutron penetration was expected for the longest path lengths of about 300 mm. Sampling times of 30 minutes were used for the longest path lengths, with sampling times adjusted for locations with smaller path lengths in order to minimize experiment time while achieving similar counting statistics for all locations. The spatial variation of unstressed lattice spacing was measured in all three orientations on 3 “comb” specimens [15, 16], taken from the locations shown in Figure 5. Measurements at one location on a cube assembled from 8 smaller $2\times2\times2$ mm^3 cubes confirmed that the stresses were fully relieved in the comb. All told, the measurements on the forging used about 144 hours of beam time.

Because of the small gauge volume and the relatively weak scattering from aluminum, the diffraction patterns were analyzed using full-pattern Rietveld analysis [17, 18]. Rietveld analysis leads to the determination of an average lattice parameter, a_i, based upon all available peaks, where i indicates x, y or z directions.

The comb results indicated that the unstressed spacings varied by as much as 870 $\mu\varepsilon$ over the y-direction of the forging with variation between the combs taken at the two ends of the block up to 500 $\mu\varepsilon$ but more typically 100 $\mu\varepsilon$. Large variations in unstressed spacing have been previously observed in 7000 series forgings [19]. Rather than interpolating in the z-direction, the results from the multiple combs were averaged and then linearly interpolated in the y-direction to define an appropriate unstressed lattice spacing corresponding to each measurement location in the block and for each direction.

Elastic strains in each coordinate direction in the sample were calculated by comparing the measured lattice parameter to the unstressed parameter. The overall strain range in the part was about 2500 με. Hooke's law for isotropic elasticity was used to calculate stresses from the strains.

Uncertainty estimates made use of some additional information. Typical strain uncertainties calculated from the Rietveld refinement were about 40-100 με for the scans and 25 με for the d_0 combs, which would translate to stress uncertainties of about ± 6-13 MPa [20, 21]. Because of additional measurements taken at ± 45 degrees in the *x*-*y* plane there were 4 strains determined in the *x*-*y* plane, but only three strains in a plane are independent. Consistency checks on the four indicated that strain errors were up to 200 με over large regions of the data. Therefore, stress uncertainties of ± 25 MPa were used.

The very large lattice parameter variation observed for the stress-free references is linked to a significant texture variation throughout the forging. At the center of the forging the texture is fairly strong with an about 6 times random 200 peak intensity along both the long direction and the transverse directions. However, away from the center of the forging the texture changes significantly over a very short range so that it is much more random, and then closer to the surface a strong 220 texture is observed along the x-direction. This indicates that the deformation in the forging is rather non-uniform over the cross section, with what looks like localized regions of high shear at a depth of about 25 mm under the surface. The spatial variation observed in the reference lattice parameters is in phase with the variations seen in the texture, and thus one origin of the strain variation is most likely the non-uniform degree of deformation in the forging.

5. Results

Figure 7 shows the surface-height contour maps measured on the opposing surface of the fracture. The top approximately 40% of each plot is the EDM cut surface and the remainder is the fracture surface. The total height range of each surface is about 2.1 mm. The plots show extensive fine detail in the fracture region but also show that high regions in the fracture region on one surface are generally mirrored by low regions in the opposing surface, as expected.

Figure 8 shows the half-misfit between the fracture surfaces as determined by averaging the two surfaces from Figure 7. The averaging of the mating fracture surface shapes results in a smooth misfit shape with a central region of lower height surrounded by higher regions. The height range is reduced to about 0.6 mm. The fracture surface portion of the misfit still shows some of the fine detail from the fracture surface, indicating a slightly imperfect fit between the two surface contours. A slight discontinuity at $z \approx 135$ mm indicates some artifact from the EDM cutting. Neither the fracture surface detail nor the EDM artifact warrant further consideration, since they are both small enough to be handled during the data smoothing.

Figure 9 shows a lineout at $z = 100$ mm from the surface averaging process. Both long range shape along *y* (order 10 mm, Figure 9a) and finer details (order 1 mm and slightly less, Figure 9b) show the expected matching between the two sides and tend to average away.

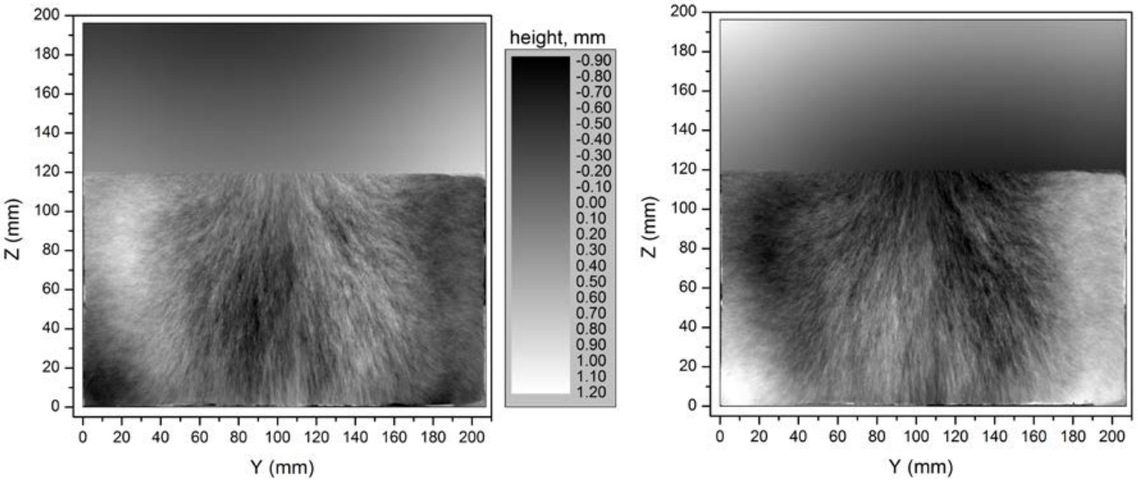

Figure 7. Measured surface height maps for the two opposing surfaces from the fracture. The bottom ≈ 120 mm of each figure is the fracture surface, the top portion is the EDM cut surface.

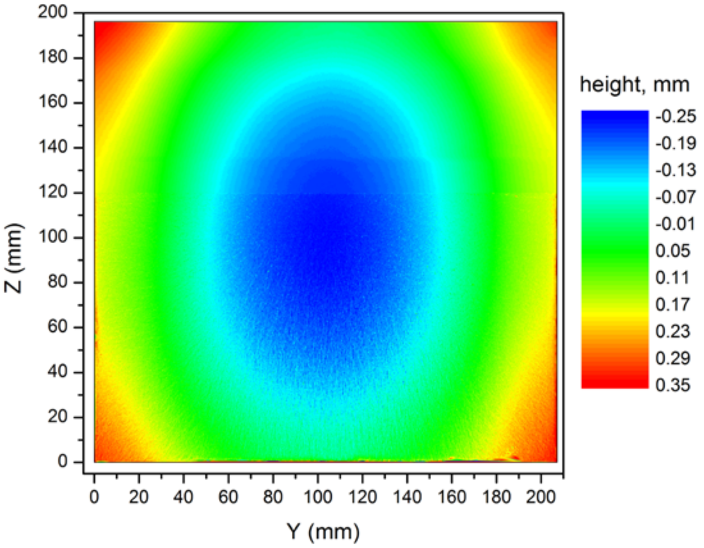

Figure 8. The half-misfit between the fracture surfaces as determined by averaging the two surfaces in Figure 7. Note that the scale is reduced relative to Figure 7.

Figure 9 also shows the corresponding lineout from the smooth surface fitted to the data. The optimal spline smoothed surface used 5 knots in each direction, which was more than sufficient to capture the shape of Figure 8. The smooth surface fit the data with a root-mean-square misfit of 0.019 mm, which corresponds to the noise level for the average surface in Figure 9. To reduce the influence of surface fitting details on the results, the stresses were calculated using 4, 5, and 6 knots in each direction and the results averaged.

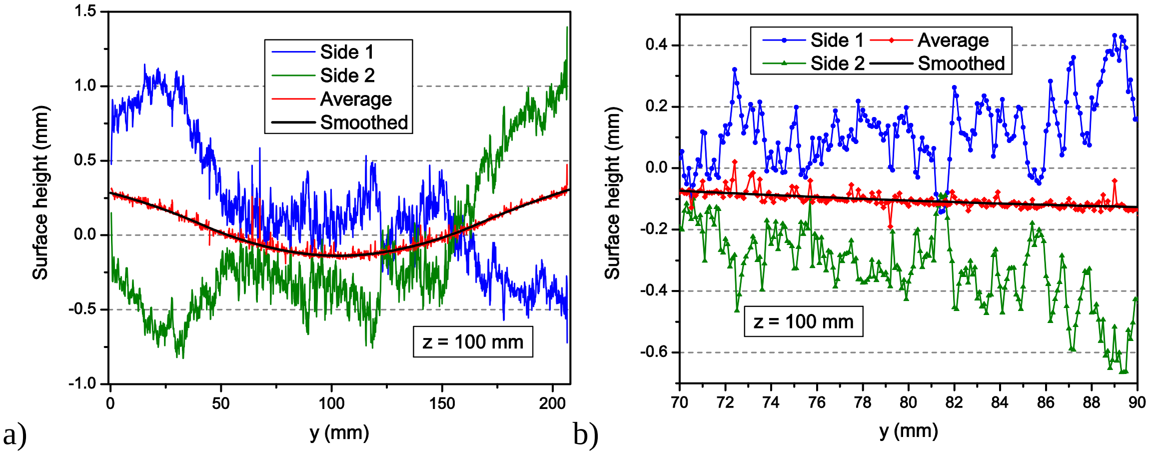

Figure 9. a) lineout at z = 100 mm from the contours in Figure 7 and Figure 8 showing how the fracture surface geometric features average away. b) Zoomed in to show finer detail.

Figure 10 shows the fracture-surface determined stress state of the specimen prior to EDM cutting. The stresses at the core of the specimen are tensile, peaking at just over 200 MPa. Balancing compressive stresses surround the tensile core reaching a maximum compression of almost 300 MPa in the corners.

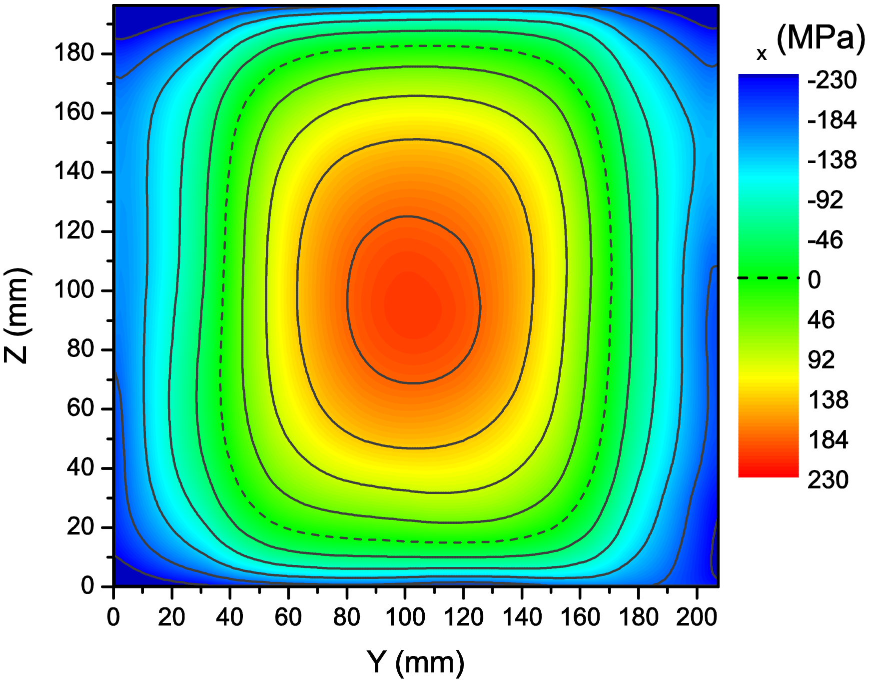

Figure 10. Original residual stresses over the fracture plane, as determined from the measured misfit between the surfaces

Figure 11 shows the validation of the fracture-surface determined stresses by the neutron diffraction measurements on the other section of the forging. The stresses from Figure 10 were extracted along the neutron scan lines shown in Figure 5 and plotted as lines to compare with the neutron data points. The spatial dimensions are normalized by the dimensions of the cross section to simplify the presentation. To avoid clutter in the plot, the neutron uncertainty bars are only shown on a single representative data point. The agreement between the neutron results and the fracture results are generally excellent, agreeing within uncertainty bars at about 95% of the neutron measurement locations, which is significantly better agreement than is expected for the one standard deviation error bars. Although within uncertainty bars, the neutron results tend to be about 10% lower than the fracture results over the central 20% of the specimen. That is the region with a strong 200 texture in the forging. For aluminum, the 200 reflection is maybe the least representative of the macroscopic stresses [22, 23], and overweighting it in the Rietveld refinement could explain the discrepancy. Also, the central region has the lowest neutron penetration and therefore the worst counting statistics. The other region with disagreement is near the specimen edges, where there was also higher texture in the forging and where a few points have the fracture surface results showing deeper compression.

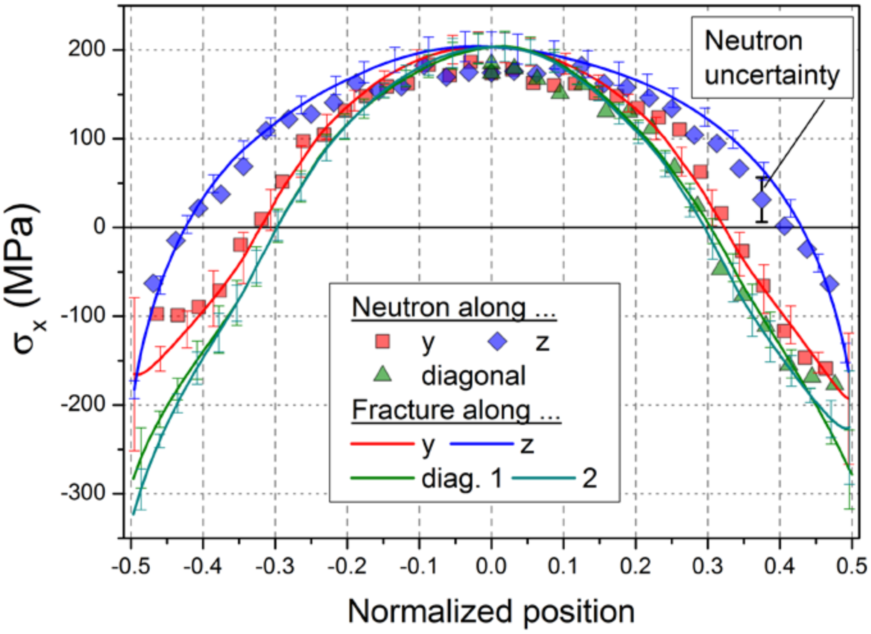

Figure 11. Residual stress along scan lines shown in Figure 5 showing that the neutron diffraction results agree very well with those from the fracture surface mismatch (Figure 10).

6. Discussion

6.1. Stresses and Fracture

The residual stress magnitudes in Figure 10 and Figure 11 are consistent with other measurements of as-quenched stresses in large forgings or thick plates of 7000 series aluminum alloys [24, 25]. During quenching, the core of the forging is the last region to cool. As the core cools it tries to contract, pulls the cooler and stronger outer shell into compression, and is left in tension by the restraint of the outer shell.

Figure 10 and Figure 11 show much deeper compressive stresses on the ±*y* edges of the specimen than on the ±*z* edges. Referring to Figure 5, the ±*y* edges of the specimen were free surfaces in the original forging and therefore had compressive stresses from the quenching process. Based on the uniform processing of the forging, the stresses along the *y*-direction (*y*-profile in Figure 11) would have been expected to exist approximately constantly along the length of the forging, except near the ends. The ±*z* edges were created when the specimen was cut from the forging, and therefore have a stress distribution resulting from the elastic relaxation of σ_z on those edges and the accompanying redistribution of the other stresses [26]. The peak compressive stresses of almost -300 MPa in the corners of Figure 10 are therefore also an effect of the stress redistribution, and the forging did not likely have such compressive stress magnitudes prior to cutting.

An FE analysis was performed to determine whether the residual stresses determined by the fracture surface analysis, and shown in Figure 10, are consistent with a fracture prediction based on linear elastic fracture mechanics (LEFM). A preliminary analysis like that in Figure 4 did not reveal sufficient cut tip loading to explain the fracture. Further consideration indicated cut closure as the likely explanation, requiring a more sophisticated analysis. The FE model, shown in Figure 12 for the 70 mm cut depth case, reflected the geometry of the removed and partially cut block just prior to fracture, with half-symmetry about the cut/fracture plane. Elastic properties for 7050-T74 were taken as an elastic modulus of 71.7 GPa and Poisson's ratio of 0.33. The mesh consisted of 8-noded, linear-displacement, hexahedral elements, with a refined mesh focused to a quarter circle at the cut tip. The quarter circle, cut-tip radius was 0.125 mm, equal to half the EDM wire diameter, and the mesh left a gap of 0.125 mm between the symmetry plane and the cut face to reflect half the EDM cut width. Symmetric boundary conditions were applied to uncut material, ahead of the cut tip on the symmetry plane. Stress from Figure 10 was applied as distributed pressure on the cut face, and the analysis included a frictionless contact condition so that the cut face was not allowed to pass the symmetry plane. Figure 12 shows significant closure over a substantial region of the top corners of the cut surface. The interaction integral method was employed to calculate the stress intensity factor, K_I, at several locations along the cut/crack front. The results provided K_I at each position along the front for a number of (20) integration domains, with each domain having increasing volume (i.e., subsequent domains included the prior domain and additional elements surrounding it). A single value of K_I at each position was selected by finding a plateau of K_I with increasing domain size; in the region of the plateau, K_I values were consistent within 0.1%.

The LEFM analysis was repeated for three cut depths, a = 60, 70, and 80 mm, where fracture occurred near a cut depth of 76.5 mm, and results from the analysis are show in Figure 13. Near the middle of the cut front, the stress intensity factor is large and positive, with peak values of 22 and 38 MPa $m^{0.5}$ at cut depths of 60 and 80 mm, respectively. Typical values of plane strain fracture toughness K_{IC} for 7050 T74 range from 20 to 40 MPa $m^{0.5}$ [27-30], with representative values shown in Table 1, which suggests fracture at a cut depth between 60 and 80 mm. This range is in good agreement with the observed fracture cut depth of 76.5 mm. A subsequent analysis was performed without contact, so that the cut face was allowed to pass the symmetry plane, which showed that cut face contact has a significant effect on the computed values of K_I (Figure 13).

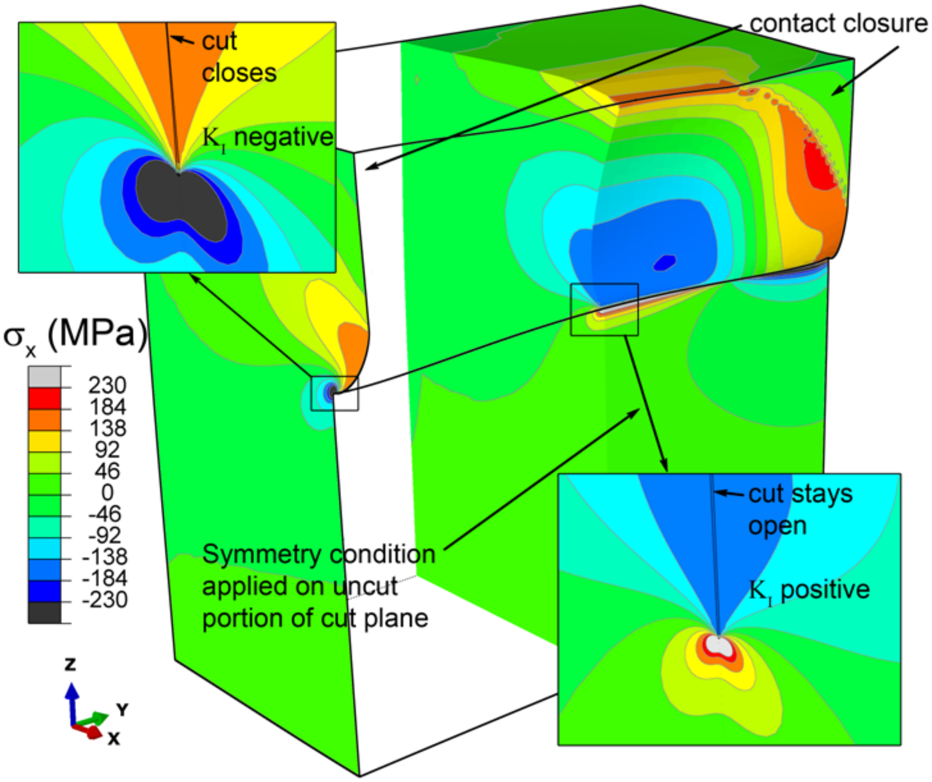

Figure 12. Half-symmetry FE model of deformations and closure region during the wire EDM cut. Deformations scaled by factor of 100 and some sections removed to show internal stresses. Inset plots of cut tips are reflected to show both sides of symmetry plane and deformation scale factor is one.

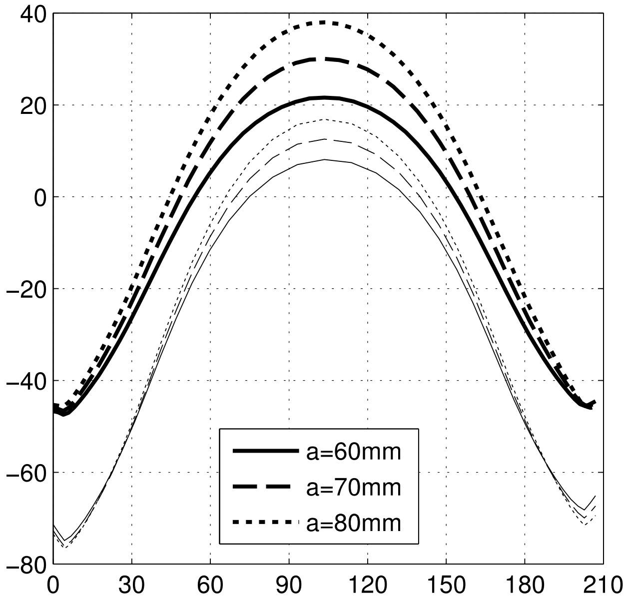

Figure 13. Stress intensity factor along the crack front, computed for three different cut depths and analyses that included and ignored cut-face contact.

Alloy/Temper	Product Form	Orientation	K_{IC}, MPa-m$^{0.5}$			Ref
			Max	Avg	Min	
7050-T74	Die Forging	S-L	30	26	23	[28]
7050-T7451	Plate	L-T	43	35	27	[28-30]
7050-T7451	Plate	T-L	42	31	23	[28-30]
7050-T7451	Plate	S-L	31	25	23	[27-30]
7050-T7452	Hand Forging	L-T	37	34	29	[28, 29]
7050-T7452	Hand Forging	T-L	24	23	20	[28, 29]
7050-T7452	Hand Forging	S-L	23	21	18	[28]

Table 1. Typical values of plane strain fracture toughness K_{IC} for Alloy 7050.

The two cuts to initially remove the specimen from the forging, Figure 5, cut through the deeper compressive stress region left by the original quenching process. Therefore, the peak K_I during those cuts was too low to cause fracture. Knowledge of residual stress has been used successfully in the past to develop successful strategies for cutting brittle parts without fracture [31]. Fracture of the specimen in this paper probably could have been avoided if the final cut had been taken at a 90 degree angle, cutting in the $\pm y$ direction instead of $-z$.

6.2. Methodology and future applications

A key assumption of the fracture-surface residual-stress determination is that the stress relaxation is elastic. Aluminum generally exhibits low-energy, ductile failure, yet the residual stress results agreed very well with the neutron diffraction measurements, which were taken on a specimen without the relaxations that might cause plasticity. Based on the K_I magnitude of about 30 MPa-m^{½}, the plastic zone size for plane-strain conditions based on static crack-tip stress fields and a typical quasi-static flow strength of 450 MPa would be about 0.7 mm [32], which is about the same as the measured half-misfit. However, even under the modestly dynamic rates of a spontaneous fracture, the stress fields are considerably different, the yield strength increases, and the plastic zone size and accompanying plastic strains are likely to be an order of magnitude or more lower [33]. The surface mismatch is an integrated effect of all of the elastic and plastic strains from relaxation, so errors that may arise from plasticity would depend on the size of the plastic zone relative to the region of elastic relaxation and also on the magnitude of plastic strains. In the forging application, the total effect was not significant. Further studies would be required to establish detailed guidance on the conditions when plasticity effects would be significant.

The practicality of the fracture surface approach for broader application will depend partly on the mismatch being measureable over other features on the fracture surface, as illustrated in Figure 9. The aluminum forging studied in this paper was ideal in one respect: the mismatch was very large at about 600 μm range. The large mismatch was a result of the large stress magnitude relative to the elastic modulus, $\sigma_{peak}/E \approx 0.3\%$, and the large part size. Based on the signal to noise of the mismatch in Figure 8 and Figure 9, at least an order of magnitude less than the current mismatch should be possible to measure. With the contour method for residual stress measurement, good results on an EDM surface have been obtained for contours with a range smaller than of 20 μm[10, 34-

36], and opposing EDM surfaces have uncorrelated roughness features which cannot average away.

The practicality of the fracture surface mismatch approach will also depend on some fracture details. A less planar fracture might cause some additional difficulty, but Bueckner's principle still applies. The surface must also be not so corroded or damaged by compressive loads as to lose the relevant geometry.

Transverse (i.e., in-plane) mismatch from surface misalignment or from the release of shear stresses can affect the measurement of mismatch in the normal direction for locally sloped surfaces. Any local fracture feature will have surface sloped positively and negatively on either side of the feature, which cause errors of opposite sign. Therefore, when the transverse mismatch magnitude approaches the wavelength of the fracture surface geometrical detail, the average surface (half-mismatch) will have noise of the same magnitude as the fracture surface detail but will otherwise equal the mismatch of perfectly aligned surfaces. (Based on this result, the noise of ~ 0.02 mm in the average fracture surface, see Figure 8 and Figure 9, indicates misalignment of that magnitude.) Transverse mismatch from shear stresses would be of the magnitude appropriate for elastic strains, and generally too small to be significant other than adding noise.

The fracture surface approach should be more broadly applicable than spontaneous brittle fracture under only the influence of residual stresses. Under the combined action of residual stresses and applied loading, the fracture surface analysis would accurately return just the residual stresses so long as the combined loading did not cause excessive plasticity. For crack growth via fatigue or stress corrosion cracking, the final failure is often brittle, so the fracture surface mismatch analysis could determine the residual stresses immediately prior to final fracture. Residual stresses can also significantly contaminate the results of fracture toughness testing by surreptitiously adding to the applied K_I (see, e.g., [37-39]), and this technique might be applicable for evaluating the residual stress effects after the fact.

6.3. Related work

Studying the mismatch of mating fracture surfaces is not new, but previous studies had different goals and used different techniques. The earliest studies used replicates to study crack profiles at various stages of fatigue cycling [40]. The in situ replication technique limited the measurements to the specimen sides, and it was used to look at in plane (y direction in Figure 1, mode II type deformation) mismatch of the surfaces to study crack closure during fatigue. Mismatch was given various physical interpretations, the most significant one being plastic deformation, and elastic relaxation of residual stresses was never considered [41].

The other major research area on mismatch is fracture surface topography analysis, sometimes called FRASTA [42, 43]. FRASTA is used to study fatigue loading [44] or ductile failure processes [45-47] where there is significant plastic deformation. The topography of conjugate fracture surfaces are measured separately, sometimes using laser scanning similar to the technique in this paper [43, 48]. Incrementally separating the two topographs reveals the local fracture processes, such as void growth or unbroken ligaments, and maps out the crack progression. Like the replication technique, FRASTA assumes that the entire mismatch is caused by plastic deformation.

7. Conclusions

For brittle fracture, a new method was developed to forensically determine the residual stresses that had originally existed on the fracture plane. The method was applied to a section of aluminum forging fractured while being cut in two. Surface height maps were measured on the opposing surfaces created by the fracture. Averaging the two height maps revealed the misfit between the two surfaces, which was caused by the stress relaxation from the fracture. Assuming elastic stress relaxation, a variation of Bueckner's principle was used to calculate the original residual stresses from the measured misfit. Neutron diffraction measurements taken on another section of the same forging agreed very well with the residual stresses determined from the fracture surfaces, validating the approach. The approach could in principle also be used to map residual stresses immediately prior to brittle fracture even if the original crack grew by fatigue or stress corrosion cracking.

8. Acknowledgements

The authors would like to thank Tom Holden and Don Brown for extensive consultation on texture and microstress effects in the neutron data, Jeremy Robinson of the University of Limerick for discussions on the stresses in 7000 series aluminum alloys, James Castle and The Boeing Company for providing the material and its pedigree for this paper from Boeing's internal study, and Mark James of the Alcoa Technical Center for technical discussions. Some of this work was performed at Los Alamos National Laboratory, operated by the Los Alamos National Security, LLC for the National Nuclear Security Administration of the U.S. Department of Energy under contract DE-AC52-06NA25396. This work has benefited from the use of the Lujan Neutron Scattering Center at LANSCE, which is funded by the Office of Basic Energy Sciences (DOE).

9. References

[1] Withers PJ. Residual stress and its role in failure. Reports on Progress in Physics. 2007;70:2211-64.
[2] James MN. Residual stress influences on structural reliability. Engineering Failure Analysis. 2011;18:1909-20.
[3] Shipley RJ, Becker WT. Volume 11: Failure analysis and prevention. ASM Handbook. Materials Park, OH: ASM International; 2002.
[4] Wulpi DJ. Understanding how components fail. Materials Park, OH: ASM International; 1999.
[5] Pineault JA, Belassel M, Brauss ME. X-ray diffraction residual stress measurement in failure analysis. In: Becker WT, Shipley RJ, editors. ASM Handbook, Volume 11: Failure Analysis and Prevention. Materials Park, OH: ASM International; 2002. p. 484-97.
[6] Bueckner HF. The propagation of cracks and the energy of elastic deformation. Transactions of the American Society of Mechanical Engineers. 1958;80:1225-30.
[7] Bueckner HF. Field singularities and related integral representations. In: Sih GC, editor. Mechanics of Fracture 1973. p. 239-314.
[8] Barenblatt GI. The Mathematical Theory of Equilibrium Cracks in Brittle Fracture. In: Dryden HL, von Kármán T, Kuerti G, van den Dungen FH, Howarth L, editors. Advances in Applied Mechanics: Elsevier; 1962. p. 55-129.

[9] Paris PC, Gomez MP, Anderson WE. A rational analytic theory of fatigue. Trends in Engineering, University of Washington. 1961;13:9-14.

[10] Prime MB. Cross-sectional mapping of residual stresses by measuring the surface contour after a cut. Journal of Engineering Materials and Technology. 2001;123:162-8.

[11] Pagliaro P, Prime MB, Robinson JS, Clausen B, Swenson H, Steinzig M, et al. Measuring Inaccessible Residual Stresses Using Multiple Methods and Superposition. Experimental Mechanics. 2011;51:1123-34.

[12] Prime MB, Sebring RJ, Edwards JM, Hughes DJ, Webster PJ. Laser surface-contouring and spline data-smoothing for residual stress measurement. Experimental Mechanics. 2004;44:176-84.

[13] Johnson G. Residual stress measurements using the contour method [Ph.D. Dissertation]: University of Manchester; 2008.

[14] Bourke MAM, Dunand DC, Ustundag E. SMARTS-A spectrometer for strain measurement in engineering materials. Applied Physics A: Materials Science & Processing. 2002;74:1707-9.

[15] Paradowska A, Finlayson TR, Price JWH, Ibrahim R, Steuwer A, Ripley M. Investigation of reference samples for residual strain measurements in a welded specimen by neutron and synchrotron X-ray diffraction. Physica B-Condensed Matter. 2006;385-86:904-7.

[16] Woo W, Em V, Hubbard CR, Lee H-J, Park KS. Residual stress determination in a dissimilar weld overlay pipe by neutron diffraction. Materials Science & Engineering: A. 2011;528:8021-7.

[17] Rietveld HM. A profile refinement method for nuclear and magnetic structures. Journal of Applied Crystallography. 1969;2:65-71.

[18] Von Dreele RB, Jorgensen JD, Windsor CG. Rietveld refinement with spallation neutron powder diffraction data. Journal of Applied Crystallography. 1982;15:581-9.

[19] Robinson JS, Tanner DA, Truman CE, Paradowska AM, Wimpory RC. The influence of quench sensitivity on residual stresses in the aluminium alloys 7010 and 7075. Materials Characterization. 2012;65:73-85.

[20] Wimpory RC, Ohms C, Hofmann M, Schneider R, Youtsos AG. Statistical analysis of residual stress determinations using neutron diffraction. International Journal of Pressure Vessels and Piping. 2009;86:48-62.

[21] Wimpory RC, Ohms C, Hofmann M, Schneider R, Youtsos AG. Corrigendum to “Statistical analysis of residual stress determinations using neutron diffraction” [International Journal of Pressure Vessels and Piping 86(1) 48–62]. International Journal of Pressure Vessels and Piping. 2009;86:721.

[22] Pang JWL, Holden TM, Mason TE. In situ generation of intergranular strains in an Al7050 alloy. Acta Materialia. 1998;46:1503-18.

[23] Clausen B, Leffers T, Lorentzen T. On the proper selection of reflections for the measurement of bulk residual stresses by diffraction methods. Acta Materialia. 2003;51:6181-8.

[24] Robinson JS, Hossain S, Truman CE, Paradowska AM, Hughes DJ, Wimpory RC, et al. Residual stress in 7449 aluminium alloy forgings. Materials Science and Engineering: A. 2010;527:2603-12.

[25] Yazdi SR, Retraint D, Lu J. Study of through-thickness residual stress by numerical and experimental techniques. Journal of Strain Analysis for Engineering Design. 1998;33:449-58.
[26] Prime MB. Residual Stresses Measured in Quenched HSLA-100 Steel Plate. SEM Annual Conference and Exposition on Experimental and Applied Mechanics. Portland, OR, USA2005. p. CD ROM paper 52
[27] Alloy 7050 Plate and Sheet. Alcoa Mill Products,. Inc. Bettendorf, Iowa.2013. www.alcoa.com/mill_products/catalog/pdf/alloy7050techsheetrev.pdf
[28] Military Standardization Handbook: Metallic Materials and Elements for Aerospace Vehicle Structures. United States Dept. of Defense. 2003. MIL-HDBK-5J:3-7–3-15.
[29] Kaufman JG. Fracture resistance of aluminum alloys: Notch toughness, tear resistance, and fracture toughness. Materials Park, OH, USA: ASM International; 2001.
[30] Aluminum standards and data. Arlington, VA, USA: The Aluminum Association; 2009.
[31] DeWald AT, Rankin JE, Hill MR, Schaffers KI. An improved cutting plan for removing laser amplifier slabs from Yb:S-FAP single crystals using residual stress measurement and finite element modeling. Journal of Crystal Growth. 2004;265:627-41.
[32] Tada H, Paris PC, Irwin GR. The stress analysis of cracks handbook 3rd ed. New York, NY: The American Society of Mechanical Engineers; 2000.
[33] Freund LB. Dynamic fracture mechanics: Cambridge University Press; 1998.
[34] Prime MB, Gnaupel-Herold T, Baumann JA, Lederich RJ, Bowden DM, Sebring RJ. Residual stress measurements in a thick, dissimilar aluminum alloy friction stir weld. Acta Materialia. 2006;54:4013-21.
[35] Kartal ME, Liljedahl CDM, Gungor S, Edwards L, Fitzpatrick ME. Determination of the profile of the complete residual stress tensor in a VPPA weld using the multi-axial contour method. Acta Materialia. 2008;56:4417-28.
[36] Pagliaro P, Prime MB, Swenson H, Zuccarello B. Measuring Multiple Residual-Stress Components Using the Contour Method and Multiple Cuts. Experimental Mechanics. 2010;50:187-94.
[37] VanDalen JE, Hill MR. Evaluation of residual stress corrections to fracture toughness values. Journal of ASTM International. 2008;5:JAI101713.
[38] Chung TJ, Neubrand A, Rodel J. Effect of residual stress on the fracture toughness of Al2O3/Al gradient materials. Key Engineering Materials. 2002;206-213:965-8.
[39] Godse R, Gurland J, Suresh S. Effects of Residual-Stresses in Fracture-Toughness Testing of Hard Metals. Materials Science and Engineering A. 1988;106:383-7.
[40] Walker N, Beevers CJ. Fatigue crack closure mechanism in titanium. Fatigue of Engineering Materials and Structures. 1979;1:135-48.
[41] Suresh S. Fatigue crack deflection and fracture surface contact: micromechanical models. Metallurgical Transactions A. 1985;16:249-60.
[42] Kobayashi T, Shockey DA. A fractographic investigation of thermal embrittlement in cast duplex stainless-steel. Metallurgical Transactions A-Physical Metallurgy and Materials Science. 1987;18:1941-9.
[43] Kobayashi T, Shockey DA. Fracture surface topography analysis (FRASTA)-Development, accomplishments, and future applications. Engineering Fracture Mechanics. 2010;77:2370-84.

[44] Kobayashi T, Shockey DA, Schmidt CG, Klopp RW. Assessment of fatigue load spectrum from fracture surface topography. International Journal of Fatigue. 1997;19:237-44.
[45] Miyamoto H, Kikuchi M, Kawazoe T. A study on the ductile fracture of Al-alloys 7075 and 2017. International Journal of Fracture. 1990;42:389-404.
[46] Bouchaud E, Boivin D, Pouchou JL, Bonamy D, Poon B, Ravichandran G. Fracture through cavitation in a metallic glass. EPL. 2008;83:66006.
[47] Stampfl J, Scherer S, Gruber M, Kolednik O. Reconstruction of surface topographies by scanning electron microscopy for application in fracture research. Applied Physics A: Materials Science & Processing. 1996;63:341-6.
[48] Ogura K, Miyoshi Y, Nishikawa I. New developments in fracture surface-analysis using x-ray and laser. JSME International Journal Series I. 1990;33:119-27.